Chapter 7

Cavity Q, Mode Volume, and Lasing Threshold in Small Diameter Microdisks with Embedded Quantum Dots

In this chapter, we continue our study of taper-coupled microdisk-QD structures by considering device performance as the disks are scaled down in size. In section 7.1, we use finite element simulations to examine the behavior of Q and V_{eff} as a function of disk diameter. We relate these parameters to those used in cQED, and from this, determine that disks of 1.5-2 μm in diameter are optimal for use in future experiments with InAs QDs. In sections 7.2 and 7.3, we present experimental measurements of fabricated devices. Through passive characterization (section 7.2), cavity Qs as high as 1.2×10^5 are demonstrated for devices with a predicted $V_{\text{eff}} \sim 2.2(\lambda/n)^3$. In addition, photoluminescence measurements (section 7.3) show that the devices operate as lasers with room temperature (RT), continuous-wave thresholds of $\sim$1 μW of absorbed pump power. Finally, the optical fiber taper is used to increase the efficiency of out-coupling by nearly two orders of magnitude, so that an overall fiber-coupled laser differential efficiency of $\xi \sim 16\%$ is achieved. We conclude by presenting some estimates of the number of QDs contributing to lasing and the spontaneous emission coupling factor (β) of the devices. The majority of this chapter is based on ref. [76].

7.1 Simulations

As described in chapter 5, finite-element eigenfrequency simulations [136, 128] using the Comsol FEMLAB software are used to study the radiation-limited quality factor (Q_{rad}) and mode volume (V_{eff}) of the microdisk cavities. Here, we consider how these parameters scale as a function of the disk size.

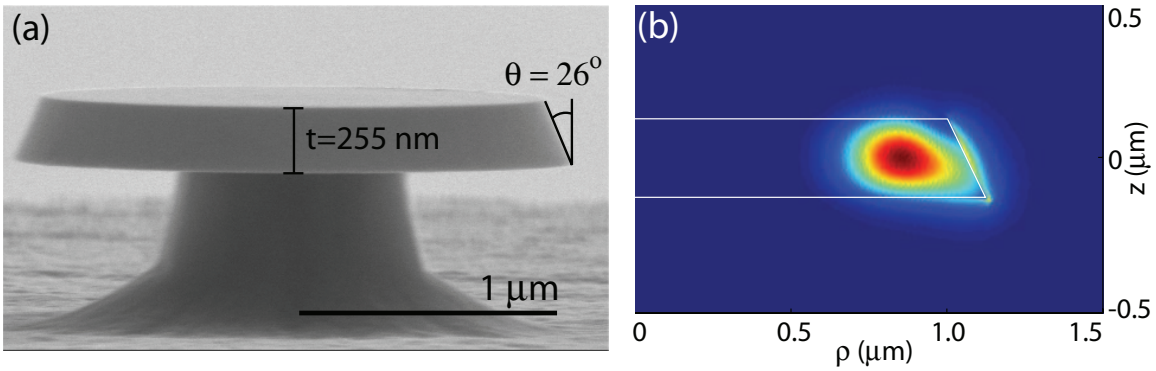

Figure 7.1: (a) Scanning electron microscope (SEM) image of a fabricated microdisk device. The disk thickness t=255 nm and sidewall angle $\theta = 26^\circ$ from vertical are taken as fixed in the finite-element simulations presented in the work. The measured average diameter for this device (i.e., the diameter at the center of the slab) is ~ 2.12 μm. (b) Finite-element-calculated $|\mathbf{E}|^2$ distribution for the $\mathrm{TE}_{p=1,m=11}$ WGM of a microdisk with a diameter of ~ 2.12 μm at the center of the slab. For this mode, $\lambda \sim 1265.41$ nm, $Q_{\mathrm{rad}} \sim 10^7$, and $V_{\mathrm{eff}} \sim 2.8(\lambda/n)^3$.

Figure 7.1(a) shows a scanning electron microscope (SEM) image of a fabricated microdisk. The devices are formed using the same fabrication techniques discussed in chapter 5, where the emphasis of sidewall smoothness over verticality during fabrication leads to an etched sidewall angle that is approximately 26° from vertical. These parameters are included in the simulations as shown fig. 7.1(b). Here, we will focus on resonant modes in the 1200 nm wavelength band, corresponding to the low temperature (T=4 K) ground state exciton transition of the QDs, relevant for future cavity QED experiments. We confine our attention to the more localized transverse electric (TE) polarized modes of the microdisk, and only consider the first order radial modes. In what follows we use the notation $\mathrm{TE}_{p,m}$ to label whispering gallery modes (WGMs) with electric field polarization dominantly in the plane of the microdisk, radial order p, and azimuthal mode number m. The refractive index of the microdisk waveguide is taken as $n = 3.36$ in the simulations, corresponding to the average of the refractive indices of the GaAs and AlGaAs layers at $\lambda = 1200$ nm. In addition, the modes that we study are *standing wave* modes that are superpositions of the standard clockwise (CW) and counterclockwise (CCW) *traveling wave* modes typically studied in microdisks. As previously mentioned, the effective mode volume for a standing wave mode, as defined in Equation 5.9, is roughly half that of a traveling wave mode.

Figures 7.1(b) and 7.2 show the results of the finite element simulations. We see that V_{eff} for these standing wave modes can be as small as $2(\lambda/n)^3$ while maintaining $Q_{\mathrm{rad}} > 10^5$. Indeed, for

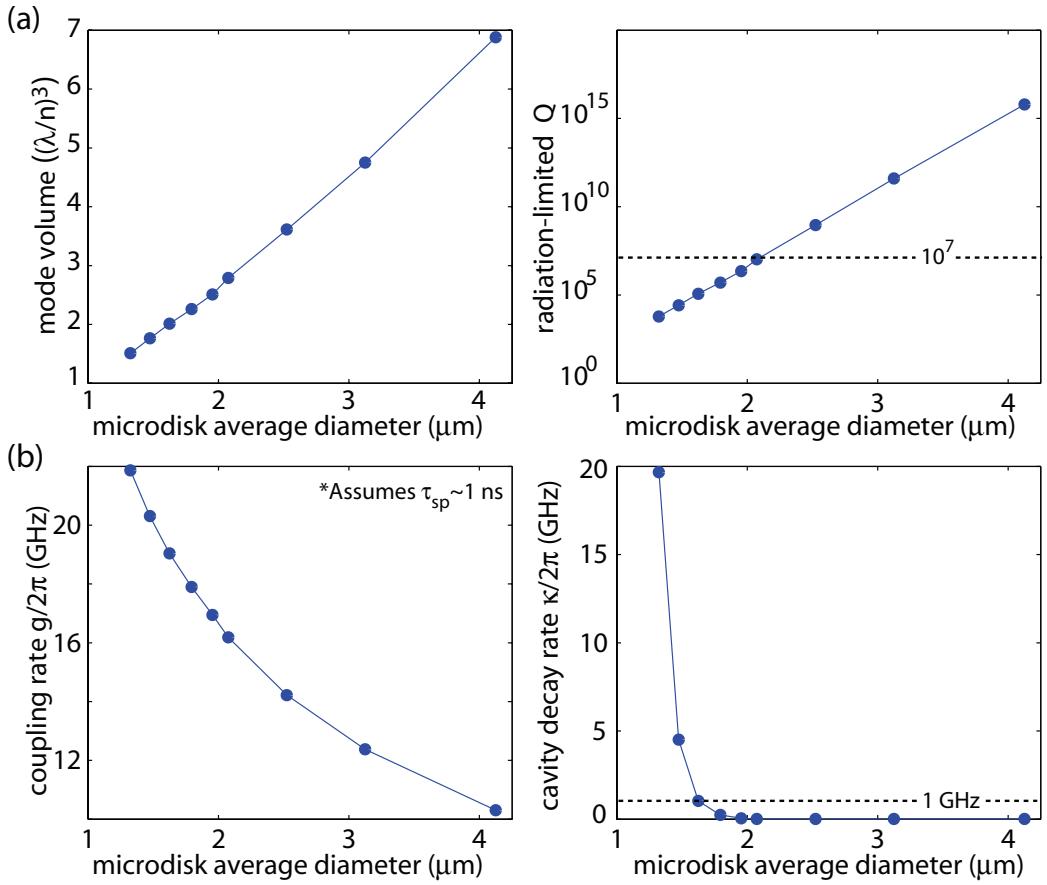

Figure 7.2: Finite-element method simulation results: (a) Modal volume V_{eff} (left) and radiation-limited cavity quality factor Q_{rad} (right) as a function of microdisk diameter (taken at the center of the slab), calculated for standing wave modes of disks of the shape shown in fig. 7.1. The modes studied are $\text{TE}_{p=1,m}$ WGMs with resonance wavelength within the 1200 nm band. (b) Coherent coupling rate $g/2\pi$ (left) and cavity decay rate $\kappa/2\pi$ (right) as a function of microdisk diameter. A QD spontaneous emission lifetime $\tau_{\text{sp}} = 1$ ns is assumed in the calculation of g.

microdisk average diameters $D > 2$ μm,[1] radiation losses are not expected to be the dominant loss mechanism as Q_{rad} quickly exceeds 10^7, and other sources of field decay such as material absorption or surface scattering are likely to dominate. To translate these results into the standard parameters studied in cavity QED, we calculate the cavity decay rate $\kappa/2\pi = \omega/(4\pi Q)$ (assuming $Q = Q_{\text{rad}}$) and the coherent coupling rate g between the cavity mode and a single QD exciton. In this calculation, a spontaneous emission lifetime $\tau_{\text{sp}} = 1$ ns is assumed for the QD exciton, and $g = \mathbf{d} \cdot \mathbf{E}/\hbar$ is the vacuum coherent coupling rate (see appendix H) between cavity mode and QD exciton, given by [9, 110]:

[1] The average diameter is taken at the center of the slab, or equivalently, is the average of the top and bottom diameters.

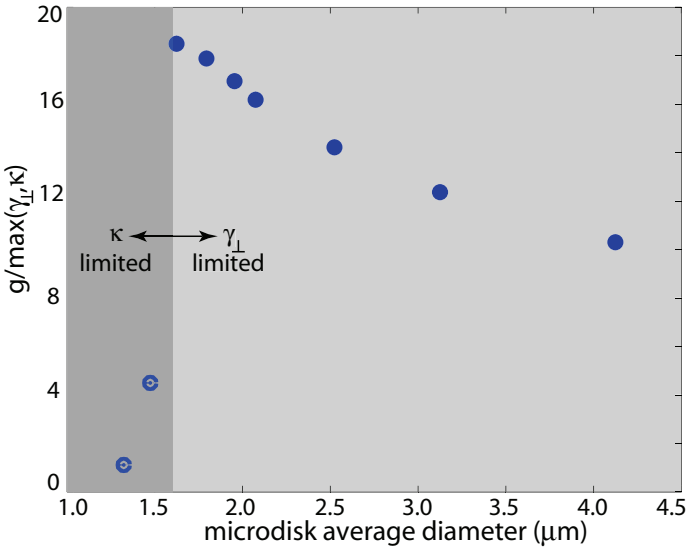

Figure 7.3: Ratio of the calculated coupling rate g to the maximum decay rate in the system, $\max(\gamma_\perp,\kappa)$, as a function of the microdisk diameter at the center of the slab. A fixed QD decay rate $\gamma_\perp/2\pi$=1 GHz is assumed, and the cavity decay rate κ is taken to be solely due to radiation loss.

$$g = \frac{1}{2\tau_{sp}}\sqrt{\frac{3c\lambda_0^2\tau_{sp}}{2\pi n^3 V_{eff}}}, \tag{7.1}$$

where c is the speed of light and n is the refractive index at the location of the QD. This formula assumes that the QD is optimally positioned within the cavity field, so that the calculated g is the maximum possible coupling rate. The resulting values for g and κ are displayed in fig. 7.2(b), and show that $g/2\pi$ can exceed $\kappa/2\pi$ by over an order of magnitude for a range of disk diameters. In addition, for all but the smallest-sized microdisks, $\kappa/2\pi < 1$ GHz. A decay rate of 1 GHz is chosen as a benchmark value as it corresponds to a linewidth of a few μeV at these wavelengths, on par with the narrowest self-assembled InAs QD exciton linewidths that have been measured at cryogenic temperatures [142]. Indeed, because dissipation in a strongly coupled QD-photon system can either be due to cavity decay or quantum dot dephasing, in fig. 7.3 we examine the ratio of g to the maximum decay rate in the system assuming a fixed QD dephasing rate $\gamma_\perp/2\pi$=1 GHz.[2] This ratio is roughly representative of the number of coherent exchanges of energy (Rabi oscillations) that can take place between QD and photon. We see that it peaks at a value of about 18 for a disk diameter $D \sim 1.5$ μm. For diameters smaller than this, loss is dominated by cavity decay due to radiation (so that $g/\max(\gamma_\perp,\kappa) = g/\kappa$), while for larger diameters, the dominant loss mechanism is due to dephasing of the QD ($g/\max(\gamma_\perp,\kappa) = g/\gamma_\perp$).

[2]Note that $\gamma_\perp$ is in general greater than half the total radiative decay rate ($\gamma_{||}/2 = 1/2\tau_{sp}$) for QD excitons, due to near-elastic scattering or dephasing events with, for example, acoustic phonons of the lattice.

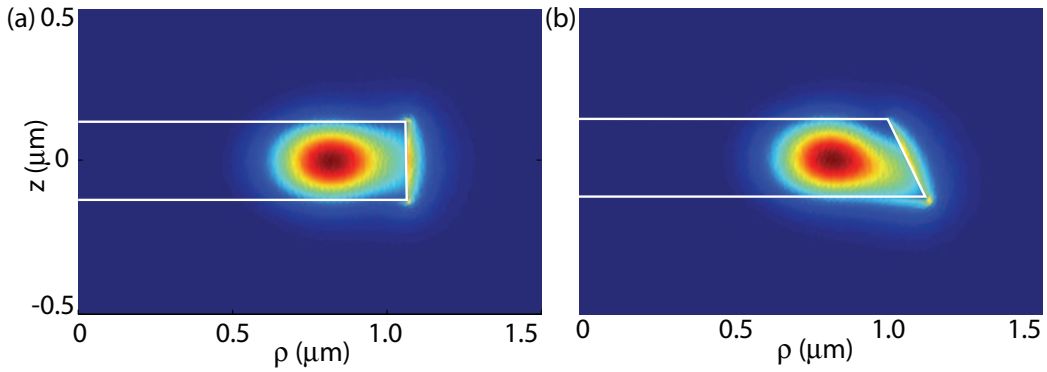

Figure 7.4: Finite-element-calculated $|\mathbf{E}|^2$ distribution for the $TE_{p=1,m=11}$ WGM in (a) microdisk with a vertical sidewall and (b) microdisk with a slanted sidewall equivalent to what has been seen in experimentally fabricated devices.

For other types of atomic-like media besides the self-assembled InAs QDs considered here one need not assume a limit of $\gamma_\perp/2\pi = 1$ GHz, and we note that due to the exponential dependence of Q_{rad} and approximately linear dependence of V_{eff} on microdisk diameter, $Q_{\text{rad}}/V_{\text{eff}}$ rapidly rises above 10^7 for microdisks of diameter $D = 2.5$ μm. These values of Q_{rad} and V_{eff} are comparable to those found in recent high-Q photonic crystal microcavity designs [21, 26, 28, 30, 27]. In fact a similar scaling for high-Q planar photonic crystal microcavities, in which one may trade off a linear increase in V_{eff} for an exponential increase in Q, has recently been described by Englund et al., in ref. [29]. For our purposes here, however, we take the ratio $g/\max(\gamma_\perp, \kappa)$ with $\gamma_\perp/2\pi = 1$ GHz as our metric, and as such focus on 1.5-2 μm diameter microdisks.

Finally, we consider what effect the sidewall angle in our structures has on Q_{rad}. To do this, we compare Q_{rad} for the slanted structure with that for a disk with a vertical sidewall and diameter equal to the average diameter of the slanted disk. Figure 7.4 compares the electric field intensity for the $TE_{1,11}$ modes in each of these structures. We find the following: for the $TE_{1,11}$ modes, the vertical disk has $\lambda_0 \sim 1262$ nm, $Q_{\text{rad}} \sim 1.4\times10^7$, and $V_{\text{eff}} \sim 2.75(\lambda/n)^3$, while the slanted disk has $\lambda_0 \sim 1265$ nm, $Q_{\text{rad}} \sim 9.8\times10^6$, and $V_{\text{eff}} \sim 2.80(\lambda/n)^3$. For the $TE_{1,9}$ modes, the vertical disk has $\lambda_0 \sim 1435$ nm, $Q_{\text{rad}} \sim 4.8\times10^5$, and $V_{\text{eff}} \sim 2.14(\lambda/n)^3$, while the slanted disk has $\lambda_0 \sim 1438$ nm, $Q_{\text{rad}} \sim 3.7\times10^5$, and $V_{\text{eff}} \sim 2.20(\lambda/n)^3$. Although Q_{rad} is indeed smaller for the slanted disks, the reduction is likely modest in comparison to the losses that would be suffered if a more vertical dry etch was employed, due to the accompanying increase in surface roughness in such an etch (appendix C).

Table 7.1: Finite-element calculated $TE_{p=1,m}$ modes of a $D = 2$ μm microdisk.

Mode label	λ_0	Q_{rad}	V_{eff}	application
$TE_{1,9}$	1438 nm	3.7×10^5	2.2 $(\lambda/n)^3$	passive RT testing
$TE_{1,10}$	1346 nm	1.9×10^6	2.5 $(\lambda/n)^3$	RT lasers
$TE_{1,11}$	1265 nm	9.8×10^6	2.8 $(\lambda/n)^3$	low-T cQED

7.2 Passive measurement of cavity Q

Similar to the devices studied in previous chapters, the samples used here were grown (by our collaborators at the University of New Mexico) through molecular beam epitaxy, and consist of a single layer of InAs QDs embedded in an $In_{0.15}Ga_{0.85}As$ quantum well, which is in turn sandwiched between layers of $Al_{0.30}Ga_{0.70}As$ and GaAs to form a 255 nm thick waveguide layer. This dot-in-a-well (DWELL) structure is grown on top of a 1.5 μm thick $Al_{0.70}Ga_{0.30}As$ buffer layer that is later undercut to form the disk pedestal. Growth parameters were adjusted [165] to put the material's RT ground state emission peak at $\lambda = 1317$ nm (fig. 7.5(a)). The basic reason for choosing a material with a red-shifted emission relative to what was used in previous investigations is to ensure that the low temperature ($\sim$10 K) emission of the QDs lies within the scan range of our 1200 nm tunable laser. This is essential for future cavity QED experiments employing near-resonant pumping of the QDs. Fabrication of the microdisk cavities follows the same process as was described in chapter 5.

We begin our measurements by using the fiber taper to passively probe the Q of the microdisks. Based on the simulations presented in section 7.1, we have focused on 2 μm diameter microdisks. Due to the small diameter of these microdisks, the finite-element-calculated free-spectral range of resonant modes is relatively large, with resonances occurring at 1265, 1346, and 1438 nm for the $TE_{p=1}$ WGMs with azimuthal mode numbers $m = 11$, 10, and 9, respectively. The simulations presented in section 7.1 were all done for the $TE_{1,11}$ mode in the $\lambda = 1200$ nm band due to the applicability of that wavelength region for future low temperature cavity QED experiments. However, for the current room-temperature measurements, the absorption due to the QD layer at those wavelengths is significant, so we probe the devices within the $\lambda = 1400$ nm band ($\sim$100 nm red detuned from the peak ground state manifold QD emission). At these longer wavelengths the radiation-limited Q_{rad} for a given disk diameter will be smaller than its value in the shorter $\lambda = 1200$ nm band. Table 7.1 summarizes the properties of the $TE_{p=1}$ WGMs within the 1200-1400 wavelength

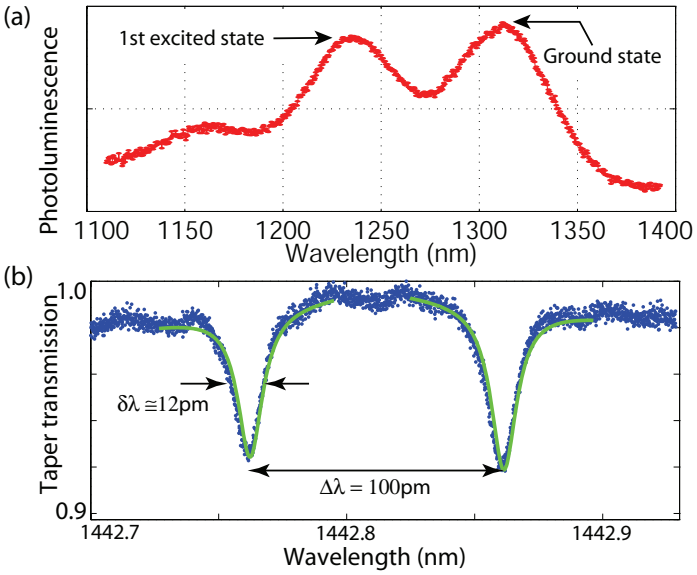

Figure 7.5: (a) Photoluminescence from an unprocessed region of the 1DWELL material whose growth has been tailored for 1.3 μm room-temperature emission. (b) Normalized transmission spectrum when a fiber taper is positioned a few hundred nm away from the edge of a $\sim$2 μm diameter microdisk fabricated from this material.

band for a $D = 2$ μm microdisk with shape as shown in fig. 7.1.

Figure 7.5(b) shows a wavelength scan of the transmitted signal when a fiber taper is positioned a few hundred nanometers away from the disk edge. The doublet resonance appearing at $\lambda \sim$ 1440 nm in the spectrum is once again the signature of the standing wave modes described earlier. The measured linewidths correspond to Q factors of 1.2×10^5, and in general, Qs of 0.9-1.3$\times10^5$ have been measured for these 2 μm diameter microdisks. The Qs of these modes are approaching the radiation-limited value of 3.7×10^5, and are some of the highest measured values for near-IR wavelength-scale microcavities in AlGaAs [71, 13, 69, 84]. The corresponding cavity decay rates are $\kappa/2\pi \sim 0.8 - 1.3$ GHz, over an order of magnitude smaller than the predicted coupling rate g for an optimally placed QD. In addition, these Qs, if replicated within the QD emission band at $\lambda = 1300$ nm are high enough to ensure that room-temperature lasing should be achievable from the single layer of QDs in these devices [165]. From calculations of the intrinsic radiation loss, the shorter 1300 nm wavelength modes should in fact have a significantly increased $Q_{\rm rad}$ of 2×10^6, although surface scattering may also slightly increase due to its approximate cubic dependence on wavelength [65].

7.3 Measurements of lasing behavior

The emission properties of the QD-containing microdisks are tested at room temperature by continuous-wave optical pumping through a high-NA objective lens at normal incidence and, initially, collecting

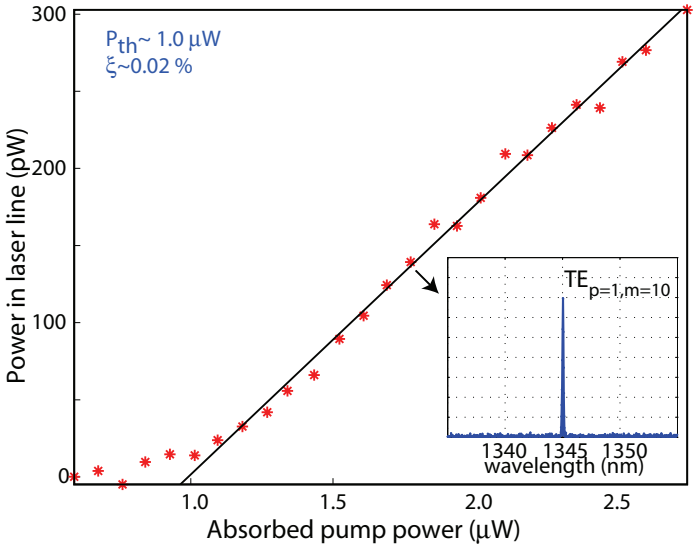

Figure 7.6: Light-in-light-out (L-L) curve for a device operated with free-space collection. The laser threshold absorbed pump power P_{th} is $\sim$1.0 μW, and its differential efficiency $\xi \sim 0.02\%$. (inset) Spectrum from the device above threshold, showing emission at $\lambda \sim 1345$ nm corresponding to the $TE_{p=1,m=10}$ WGM.

the normal incidence emitted light through the same lens. A light-in versus light-out (L-L) curve for one of the $D \sim 2$ μm microdisks with a resonant emission peak at $\lambda \sim 1345$ nm is shown in fig. 7.6, and displays a lasing threshold kink at approximately 1.0 μW of absorbed pump power. The laser mode wavelength corresponds well with the $TE_{p=1,m=10}$ mode from finite-element simulations (see table 7.1). The absorbed pump power is estimated to be 11% of the incident pump power on the microdisk, and was determined assuming an absorption coefficient of 10^4 cm^{-1} for the GaAs layers and quantum well layer. This threshold level is approximately two orders of magnitude smaller than those in recent demonstrations of RT, continuous-wave microdisk QD lasers [166, 167], although the active regions in those devices contain five stacked layers of QDs while the devices presented here contain only a single layer of QDs.

The low lasing threshold of the device presented in fig. 7.6 was consistently measured for the set of devices on this sample (approximately 20 devices). In fig. 7.7(a) we show another L-L curve, this time for a device that has a $TE_{p=1,m=10}$ WGM emission peak at $\lambda = 1330$ nm and has a threshold absorbed pump power of 1.1 μW. As described in the previous chapter and in ref. [75], the same fiber taper used to measure the cavity Q can efficiently out-couple light from the lasing mode. We do this by maintaining the free-space pumping used above while contacting a fiber taper to the side of the microdisk as shown in the inset of fig. 7.7(b). From the corresponding L-L curve (fig. 7.7(b)) we see that the laser threshold under fiber taper loading has increased from 1.1 μW to 1.6 μW, but in addition the differential laser efficiency ξ is now 4% compared to 0.1% when employing free-space collection (fig. 7.7(a)-(b)). Furthermore, because the microdisk modes are standing waves

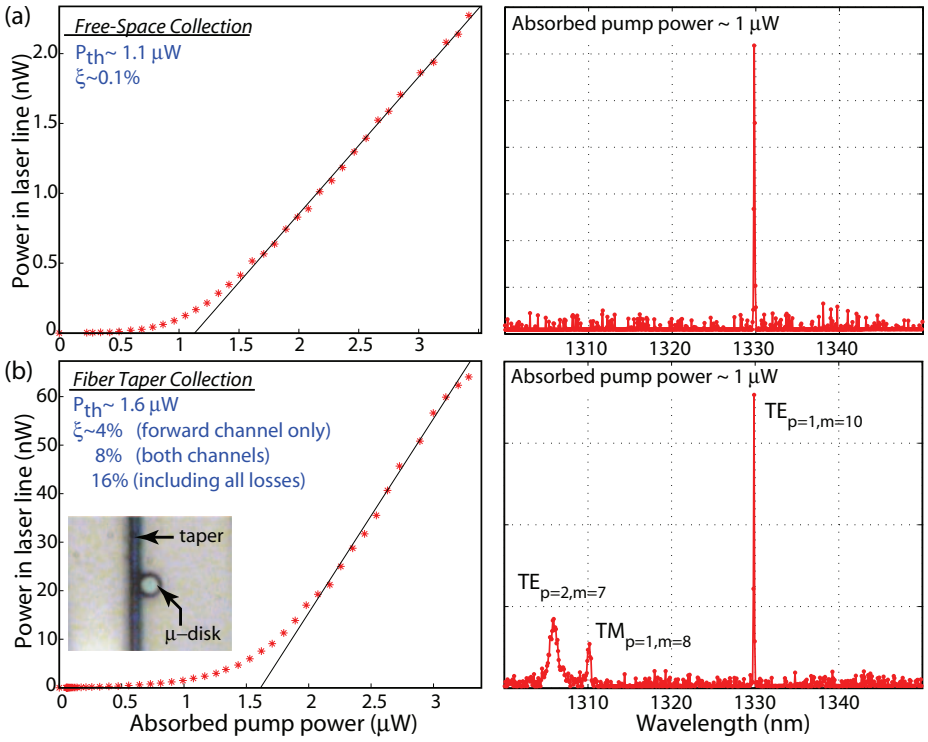

Figure 7.7: (a) (left) L-L curve for another microdisk device operated with free-space collection, with $P_{th} \sim 1.1$ μW and $\xi \sim 0.1\%$. (right) Spectrum from the device near laser threshold, showing emission at $\lambda \sim 1330$ nm. (b) (left) L-L curve for the same device using an optical fiber taper to collect the emission. P_{th} has increased to 1.6 μW while ξ increased to 4% for collection in the forward fiber taper channel. (inset) Optical microscope image of the taper output coupler aligned to the microdisk. (right) Spectrum of the fiber taper collected light below threshold.

they radiate into both the forwards and backwards channels of the fiber. With collection from both the forward and backward channels the differential efficiency was measured to be twice that of the single forward channel. Collecting from both channels and adjusting for all fiber losses in the system (roughly 50% due to fiber splices and taper loss), the total differential laser efficiency with fiber taper collection is 16%. Due to the difference in photon energy of the pump and microdisk lasers, this laser differential efficiency corresponds to a conversion efficiency of 28% from pump photons to fiber-collected microdisk laser photons. 28% is thus a *lower* bound on the fiber-taper collection efficiency and/or quantum efficiency of the QD active region.

In addition to the improved laser differential efficiency of the $TE_{p=1,m=10}$ laser mode when using the fiber taper to out-couple the laser light, we also see in the below-threshold spectrum of fig. 7.7(b) that two additional resonances appear at $\lambda = 1310$ nm and $\lambda = 1306$ nm. The long wavelength mode is identified as $TM_{p=1,m=8}$ and the short wavelength mode as $TE_{p=2,m=7}$ from finite-element

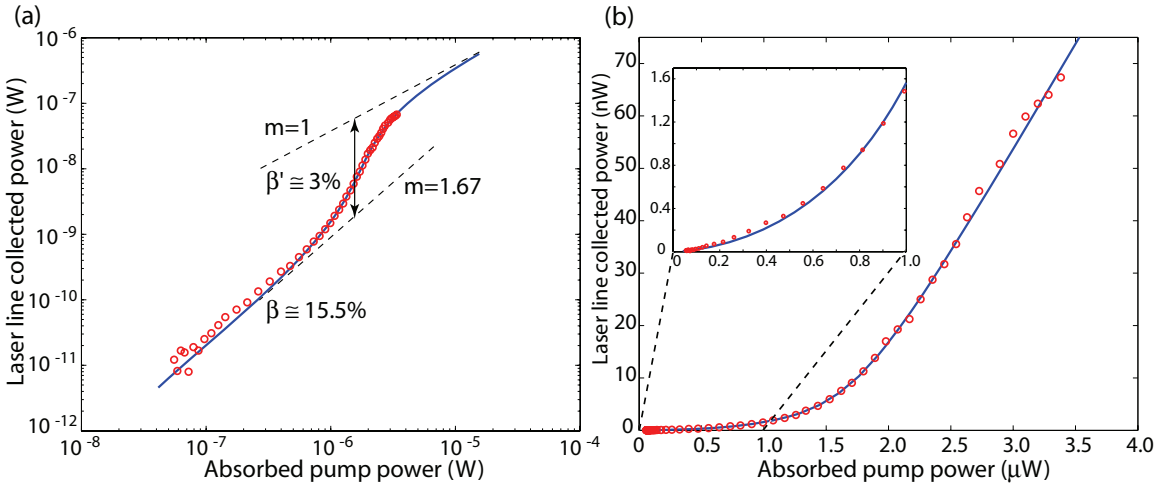

Figure 7.8: L-L curve experimental data (red circles) and rate-equation model fit (blue line) to data for the fiber taper coupled laser of fig. 7.7(b) : (a) log-log plot and (b) linear plot (inset shows deep subthreshold data and fit). $\beta' \sim 3\%$ is the spontaneous emission factor estimated directly from the slope change in the data, and thus includes a large non-radiative component, while $\beta \sim 15.5\%$ is the value used in the rate-equation model fit.

simulations. These modes are not discernible in the free-space collected spectrum due to their low radiation-limited Q factors (800 and 5000 for the $TE_{2,7}$ and $TM_{1,8}$, respectively), but show up in the taper coupled spectrum due to their alignment with the QD ground state exciton emission peak and the heightened sensitivity of the taper coupling method. The single-mode lasing and limited number of WGM resonances (6 when including the degeneracy of the WGMs) in the emission spectrum in these $D = 2$ μm microdisks is a result of the large 80-100 nm free-spectral-range of modes in the 1300-1500 wavelength band. As a result, one would expect the spontaneous emission factor (β) of these microdisk lasers to be relatively high.

A log-log plot of the fiber taper coupled laser emission of fig. 7.7(b) is shown in fig. 7.8(a) along with a rate-equation model fit to the data. Of particular note is the well defined subthreshold linear slope of the log-log plot. In this case the sensitivity of the fiber taper collection allows for the subthreshold slope to be accurately estimated at m=1.67, corresponding to a near quadratic dependence of spontaneous emission intensity on pump power (fig. 7.8(b), inset) and indicating that there is likely significant non-radiative recombination. Assuming that radiative recombination occurs as a biparticle process,[3] the larger than unity power law dependence of subthreshold emission on pump power is indicative of single-particle non-radiative recombination processes such as surface recom-

[3] As has been discussed recently in ref. [168] this may not be an accurate model for QD state filling, but for our simple analysis here it will suffice.

bination [121]. Given the close proximity of the WGM laser mode to the periphery of the microdisk and the above-band pumping, the presence of significant surface recombination is not surprising. Unfortunately, due to this large non-radiative component one can only provide a *weak lower bound* β' for the β-factor directly from the L-L curve. From fig. 7.8 we estimate $\beta \geq \beta' \sim 3\%$.

A rate-equation model (see appendix F) incorporating bi-particle spontaneous emission proportional to N^2 and surface recombination with a $N^{1.22}$ carrier dependence (the ratio of the power law dependence is set equal to the measured subthreshold slope of m=1.67) is fit to the data and shown as a solid curve in fig. 7.8. In this model the measured fiber taper collection efficiency was used, along with the previously measured and estimated QD density, maximum gain, and quantum efficiency from stripe lasers [165]. An estimate for the actual radiative β-factor of 15.5% was used, corresponding closely with the partitioning of spontaneous emission amongst the 6 localized and high-Q WGM resonances within the QD ground state manifold emission band.[4]. The reference spontaneous emission lifetime of the ground state QD exciton in bulk was taken as $\tau_{sp} = 1$ ns. The data was fit by varying *only* the effective surface recombination velocity. As seen in fig. 7.8, the fit is quite good over the entire subthreshold and threshold regions of the laser data. The inferred surface recombination velocity from the fit is $v_s \sim 75$ cm/s, extremely slow for the AlGaAs material system [152] but perhaps indicative of the fast capture rate of carriers and subsequent localization into QDs [170, 171]. Due to the large perimeter-to-area ratio in these small $D = 2$ μm microdisks, even with this low velocity the model predicts that laser threshold pump power is dominated by surface recombination with an effective lifetime $\tau_s \sim 300$ ps. Such a surface recombination lifetime has also been estimated by Ide and Baba et al., in their recent work on QD-microdisk lasers [151].

The number of QDs contributing to lasing in these small microdisks can also be estimated. From the finite-element simulations the area of the standing wave WGM lasing mode in the plane of the QD layer is approximately 1 μm^2, and the predicted QD density for this sample is 300 μm^{-2}, so that ~ 300 QDs are spatially aligned with the cavity mode. Assuming a RT homogeneous linewidth on the order of a few meV [142], compared to a measured inhomogeneous Gaussian broadening of 35 meV, and considering the location of the lasing mode in the tail of the Gaussian distribution, we estimate $< 10\%$ of these dots are spectrally aligned with the cavity mode. By this estimate, on the order of 25 QDs contribute to lasing.

[4]This estimate was based upon considering Purcell enhancement at RT for QDs spatially and spectrally aligned with the WGMs ($F_P \sim 6$), and suppression of spontaneous emission for QDs spatially and spectrally misaligned from the WGMs ($F_P \sim 0.4$) This estimate is consistent with FDTD calculations of similar sized microdisks [169].